Type II Band Alignment of NiO/α-Ga₂O₃ For Annealing Temperatures Up To 600°C

Xinyi Xia[1], Jian-Sian Li[1], Chao-Ching Chiang[1], Timothy Jinsoo Yoo[2], Eitan Hershkovitz[2], Fan Ren[1], Honggyu Kim[2], Jihyun Kim[3], Dae-Woo Jeon[4], Ji-Hyeon Park[4] and S.J. Pearton[2a)]

[1]Department of Chemical Engineering, University of Florida, Gainesville, FL 32606 USA
[2]Department of Materials Science and Engineering, University of Florida, Gainesville, FL 32606 USA
[3]School of Chemical and Biological Engineering, Seoul National University, Seoul 08826, South Korea
[4]Korea Institute of Ceramic Engineering and Technology, Jinju 52851, South Korea

[a)] Electronic mail: spear@mse.ufl.edu

There is increasing interest in the alpha polytype of Ga₂O₃ because of its even larger bandgap than the more studied beta polytype, but in common with the latter, there is no viable p-type doping technology. One option is to use p-type oxides to realize heterojunctions and NiO is one of the candidate oxides. The band alignment of sputtered NiO on α-Ga₂O₃ remains type II, staggered gap for annealing temperatures up to 600°C, showing that this a viable approach for hole injection in power electronic devices based on the alpha polytype of Ga₂O₃. The magnitude of both the conduction and valence band offsets increase with temperature up to 500°C, but then are stable to 600°C. For the as-deposited NiO/ α-Ga₂O₃ heterojunction, ΔE_V=-2.8 eV and ΔE_C= 1.6 eV, while after 600°C annealing the corresponding values are ΔE_V=-4.4 eV and ΔE_C= 3.02 eV. These values are 1-2 eV larger than for the NiO/β-Ga₂O₃ heterojunction.

I. INTRODUCTION

The thermodynamically stable form of Ga_2O_3 is the monoclinic β-phase ($C2/m$), but there are at least five other phases identified. The monoclinic β- polymorph has attracted most attention of the 6 different polymorphs of Ga_2O_3, but there is increasing interest in metastable corundum α-Ga_2O_3 due to its even larger bandgap and compatibility with growth on isomorphous sapphire (α-Al_2O_3) substrates [1-25]. The corundum α-Ga_2O_3 belongs to the trigonal R3c space group (a = 5.05952 Å, c = 13.62480 Å, α = β = γ = 120°) [3-5]. This highly asymmetric monoclinic structure leads to anisotropic materials properties and challenges in crystal growth, leading to more attention on the α-polytype, which has higher symmetry and more facile epitaxial growth conditions than β-Ga_2O_3 [1-5]. It is known that epitaxial films of α-polytype Ga_2O_3 grown on m-plane sapphire are stable up to 600 °C anneal temperatures but is metastable and converts to the β-phase after annealing at 800 °C [26], but this allows a practical window for device processing and many reports of alpha polytype devices exist.

To overcome the absence of conventional p-type dopants for α-Ga_2O_3 and be able to realize p-n junction devices, a variety of p-type oxides have been integrated with n-type Ga_2O_3. For the alpha polytype, these have included Ir_2O_3, which can be lattice-matched to α-Ga_2O_3 [27]. The band alignment of the α-Ga_2O_3/a-Ir_2O_3 heterojunction is a staggered gap, type-II, with valence- and conduction-band offsets of 3.34 eV and 1.04 eV, respectively [28]. Similarly, the band alignment of atomic layer-deposited (ALD) BeO and β-Ga_2O_3 has been reported [28]. However, for hole injection purposes, it is not necessary to have a lattice-matched layer and more common alternatives such as NiO can be considered for devices such as vertical p–n heterojunction rectifiers [29-33]. Several previous studies reported that NiO has a staggered type II alignment on β-Ga_2O_3,

allowing for efficient hole injection [29-33]. However, to date, there has been no measurement of band alignments of NiO on the other polytypes of Ga_2O_3 and especially this is important for the alpha polytype due to it large bandgap and exceptional promise for power devices with high figures-of-merit.

In this paper, we carry out a similar study for NiO on α-Ga_2O_3 and establish that there is also a type II alignment, and this remains the case up to annealing temperatures of 600°C. This is important since it covers the thermal budget of most common device processing steps and establishes NiO as a potential p-type oxide for heterojunction power devices based on α-Ga_2O_3. The thermal stability of NiO/α-Ga_2O_3 heterointerfaces is also of interest from comparing with conventional metal contacts used for Schottky rectifiers, since this is also a factor in their potential device applications.

II. EXPERIMENTAL

The α-Ga_2O_3 layers were grown by hydride vapor phase epitaxy on (0001) sapphire substrates. The growth temperature was 470°C [34]. The gaseous precursors were HCl and O_2. Pure Ga metal was used to form GaCl and $GaCl_3$ as precursors for Ga_2O_3,. These gases were transported to the reactor using with N_2 carrier gas. The thicknesses of the α-Ga_2O_3 epilayers were 1.2 μm, at a growth rate of ~6 μm/h, or growth times of the order of 10 minutes.

The properties of NiO depend on controlling the stoichiometry during deposition for as-deposited films. Our films were 6-60 nm thick and deposited by magnetron sputtering at 3mTorr and 150W of 13.56 MHz power using two targets to achieve a deposition rate around 0.2 Å.sec^{-1}. For calibration experiments, the depositions were performed onto quartz substates Since the depositions were done at room temperature

where the surface mobility is small, it is not expected that there will be much difference in the structure of the NiO deposited on quartz or Ga_2O_3. This was done to avoid complications from possible defect-related absorption in the Ga_2O_3. The Ar/O_2 ratio during sputtering was used to control the doping in the NiO at 5×10^{18} cm^{-3}, with hole mobility < 1 cm^2 $\cdot$V^{-1} s^{-1}. The temperature of the sample during deposition was $<100°C$. The bandgaps were determined for as-deposited and annealed films using UV-Vis (Perkin-Elmer Lambda 800 UV/Vis spectrometer). The absorbance spectrum were collected and Tauc plots were used to calculate the bandgap of the NiO. As summarized in a recent review [35], conflicting previous reports have interpreted the bandgap as either direct [36] or indirect [37]. Since band structure calculations show the presence of both [35], we calculated the values for both using the usual power law, $(\alpha h\nu)^n = C(h\nu - E_g)$, where α is the absorption coefficient, $h\nu$ is the photon energy, E_g is the band gap, and C is a constant. For indirect bandgaps, the exponent n is 0.5, while for direct gaps it is 2 [38,39]. The extrapolation of a linear fit on these respective Tauc plots provides the bandgap [39]. As will be seen, we found better fits for the assumption of a direct gap.

The band alignments were determined from the standard X-Ray Photoelectron Spectroscopy (XPS) method [40-43], in which the core levels and valence band maxima (VBM) positions are measured from a thick (60 nm) NiO layer and in the epitaxial α-Ga_2O_3. These same core level locations were re-measured in a NiO/α-Ga_2O_3 heterojunction consisting of 6 nm NiO sputtered on α-Ga_2O_3. The shift of the core level binding energy locations (ΔE_{CL}) within the heterostructure determines the valence band offset (ΔE_V) from [44,45]

$$\Delta E_V = \Delta E_{CL} + (E_{Core} - E_{VBM})_{Ref.\ NiO} - (E_{Core} - E_{VBM})_{Ref.\ Ga_2O_3}$$

The XPS system has been described in detail previously [29,44,45], but in brief is a Physical Instruments ULVAC PHI, with an Al x-ray source (energy 1486.6 eV, source power 300W), analysis size of 100 µm diameter, a take-off angle of 50° and acceptance angle of ±7 degrees. The electron pass energy was 23.5 eV for high-resolution scans. The total energy resolution of this XPS system is about 0.5 eV, and the accuracy of the observed binding energy is within 0.03 eV. When applied correctly [41-43], the XPS method is a reliable one for determining band offsets and avoids issues of the influence of defects states on alternative current or capacitance-based methods.

For high-angle annular dark-field (HAADF) imaging in scanning transmission electron microscopy (STEM), cross-section microscopy samples of a 300°C annealed NiO/α-Ga$_2$O$_3$ heterostructure were prepared along the [$\bar{1}$000] zone axis of α-Ga$_2$O$_3$ using a FEI Helios Dual Beam Nanolab 600 focused ion beam (FIB) system. HAADF-STEM imaging of the NiO/α-Ga$_2$O$_3$ interface structure was carried out using a 200 kV Themis Z (Thermo Scientific) equipped with a probe aberration corrector and a HAADF detector with an inner collection angle of 58 mrad.

RESULTS AND DISCUSSION

Figure 1 shows the HAADF-STEM imaging results for a 300°C annealed NiO/α-Ga$_2$O$_3$ heterostructure. Figure 1(a) is a HAADF-STEM image of the full diode structure, consisting of the top p-type NiO and bottom n-type α-Ga$_2$O$_3$, recorded along the [$\bar{1}$000] projection with respect to the trigonal α-Ga$_2$O$_3$. The high magnification HAADF-STEM image in Fig. 1(b) reveals that the NiO/α-Ga$_2$O$_3$ interface is atomically abrupt and that the α-Ga$_2$O$_3$ near the heterointerface is pristine without extended defects. The annealing strategy employed in this study is shown to be effective at relieving previously observed,

sputtering-induced damage at the interface [46]. Figures 1(c) and 1(d) are a high

magnification HAADF-STEM image and schematic of the α-Ga_2O_3 atomic structure

viewed along [$\bar{1}000$] demonstrating that the growth plane of the α-Ga_2O_3 film is (0001).

Note that due to the relatively low atomic number of oxygen (Z=8) as compared to Ga

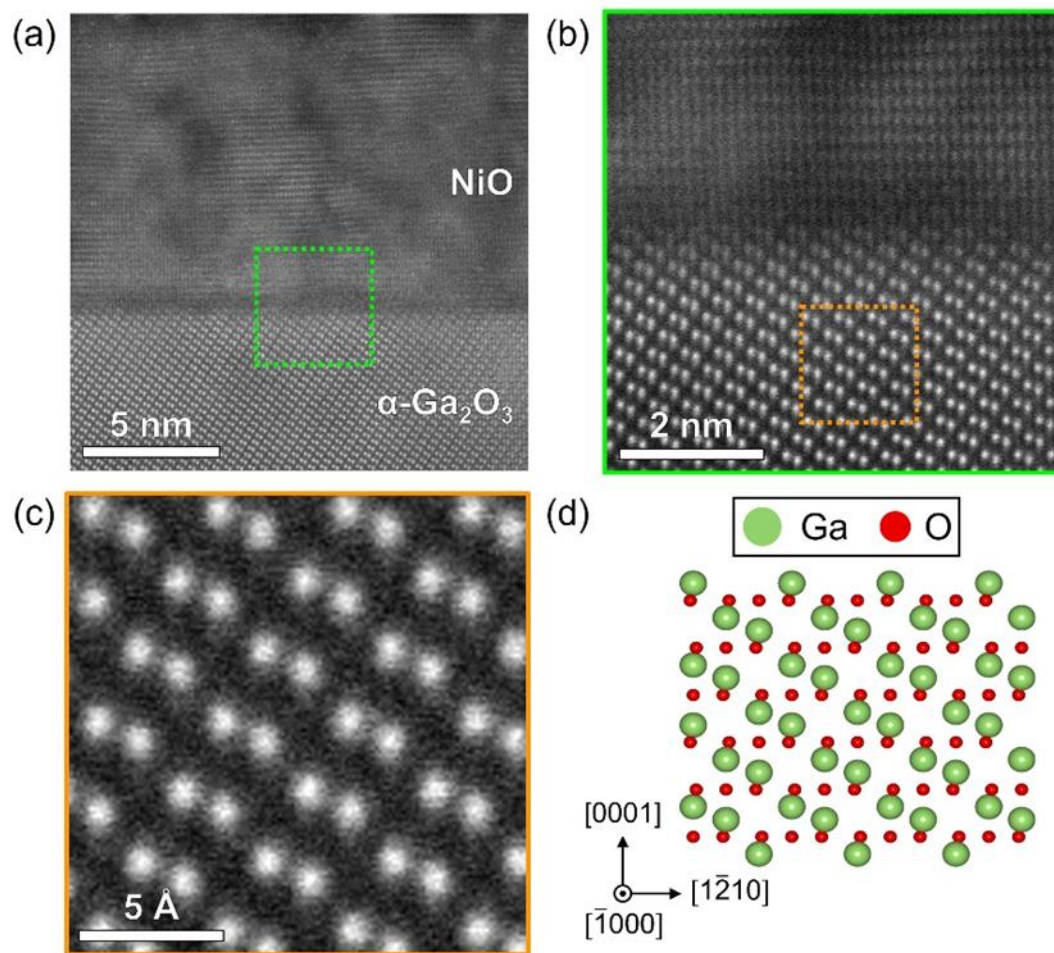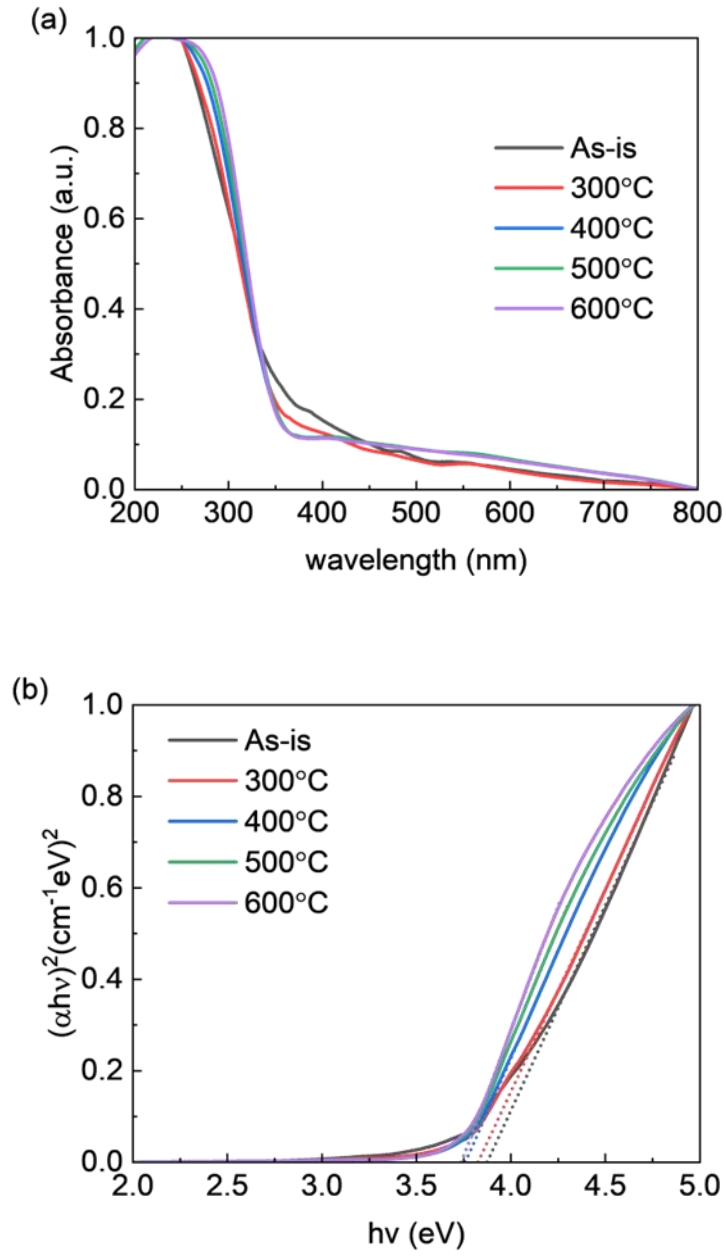(Z=31), only Ga atomic columns are visible in HAADF-STEM images.

Figure 1. (a) HAADF-STEM image of NiO/α-Ga_2O_3 heterostructure. (b) High
magnification HAADF-STEM image from the dashed green box in (a) showing that the
interface between NiO/α-Ga_2O_3 is atomically sharp. (c) HAADF-STEM image and (d)
schematic of the atomic structure of α-Ga_2O_3 outlined in the dashed orange box in (b)
revealing the [$\bar{1}000$] zone axis and the (0001) growth surface of α-Ga_2O_3.

The valence band offsets were obtained from the XPS core level shifts in the heterostructure samples, while the bandgaps of the NiO and α-Ga_2O_3 were obtained from Tauc plots and XPS and Core-valence band maxima (VBM) measurements, respectively. Knowing both the bandgaps and valence band offsets then allowed calculation of the conduction band offsets. This was done for separate layers of NiO annealed for 5 min at temperatures from 300-600°C under an O_2 ambient using Rapid Thermal Annealing (RTA). We kept the annealing ambient constant and chose O_2 to avoid possibly creating oxygen vacancies which are known to strongly influence the electrical properties of many oxides. Figure 2(a) shows Ultraviolet-Visible Spectroscopy (UV-Vis) absorption data, while the corresponding Tauc plots are shown in Figure 2(b) for power law of 2(direct gap) and in (c) for power law 0.5 (indirect gap). There is a better fit for the former. The extracted direct bandgap decreased with annealing temperature, from 3.90 eV for as-deposited films to 3.72 eV for those annealed at 600°C, as tabulated in Table 1. For completeness, we also include the results extracted if the gap is indirect and where there was a reasonable straight section of the plot to extrapolate from, with the values being ~0.5 eV smaller than the direct gaps). The bandgap of the as-deposited NiO and the small changes with annealing are consistent with the range of values reported in the literature [36]. Changes with annealing could be due to the fact that with increasing annealing temperature, more oxygen escapes from the film, corresponding to a decrease in the Ni_2O_3/NiO ratio. With an increase of annealing temperature, the bandgap decreases due to more NiO being formed relative to Ni_2O_3
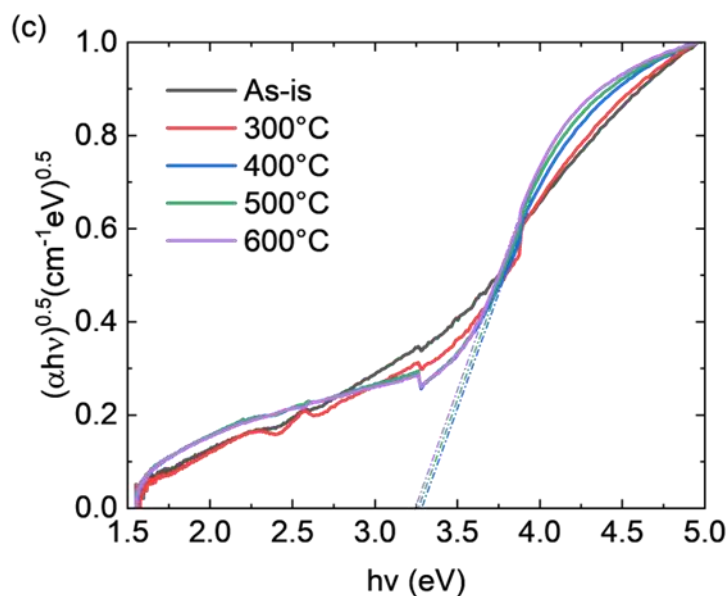
Figure 2. (a) NiO absorbance spectrum measured by UV-vis. Tauc plot for the extrapolation of (b) direct bandgaps of NiO, and (c) Indirect bandgaps of NiO as-is and annealed at different temperatures.

The bandgap of the α-Ga$_2$O$_3$ was determined using the onset of the plasmon loss feature in O 1s photoemission spectrum, as shown in Figure 3(a). The XPS spectra of core levels to valence band maximum for α-Ga$_2$O$_3$ are shown in Figure 3(b) and the values also tabulated in Table 1. Our value for the bandgap is within the reported ranges for α-Ga$_2$O$_3$ [1, 35]. We did not calculate the bandgap of α-Ga$_2$O$_3$ using a Tauc plot, because this method is less accurate for large bandgap materials, and thus we preferred the onset of the plasmon loss feature in O 1s photoemission spectrum. The α-Ga$_2$O$_3$ bandgap was independent of annealing temperature.
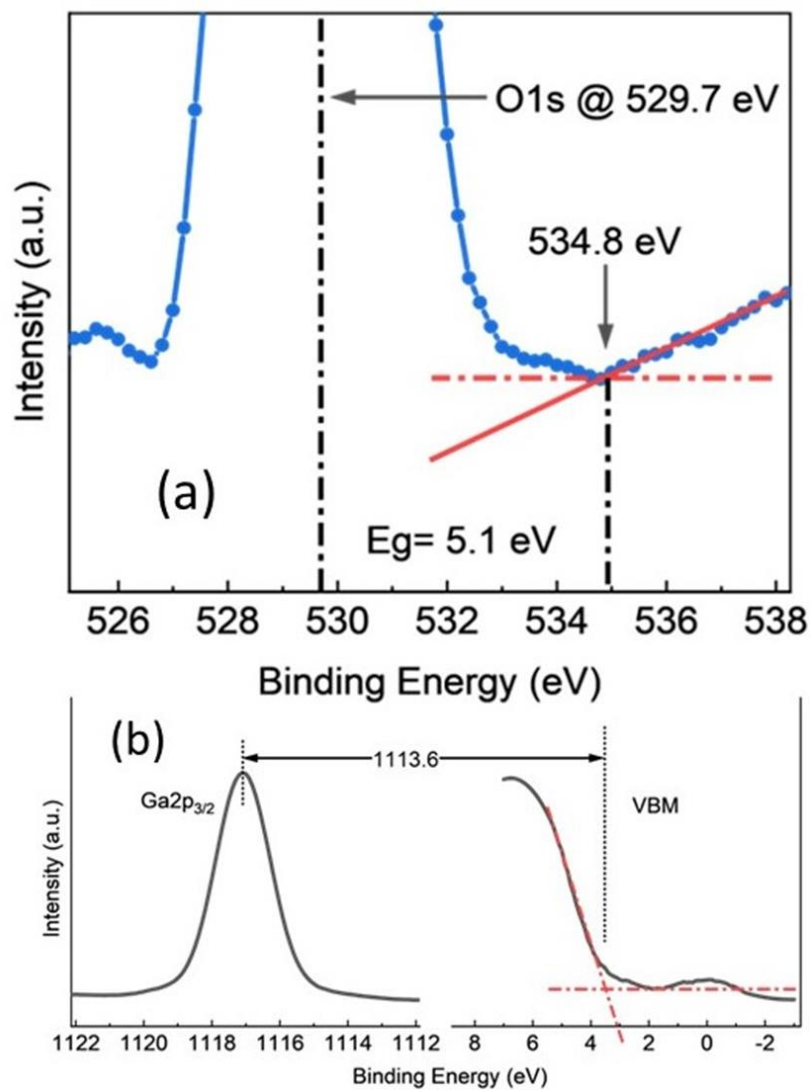
Figure 3. (a) Bandgap of α-Ga₂O₃ determined using the onset of the plasmon loss feature in O 1s photoemission spectrum (b) XPS spectra of core levels to valence band maximum for α-Ga₂O₃.

Table 1. (top) NiO bandgap measured by UV-vis and fitting to either direct or indirect bandgap. (bottom) Valence band maximum and core level data used to calculate the bandgap of α-Ga₂O₃ (bottom).

	As-is	300°C	400°C	500°C	600°C
Direct Energy Bandgap (eV)	3.90	3.84	3.76	3.74	3.72
Indirect Energy Bandgap (eV)	N/A	N/A	3.28	3.26	3.25

α-Ga₂O₃			
VBM	Core Level Peak (Ga2p$_{3/2}$)	Core - VBM	Bandgap (eV)
3.5	1117.1	1113.6	5.1

The high resolution XPS spectra for the vacuum-core delta regions of Ga₂O₃ are shown in Figure 4 for heterojunction samples annealed at different temperatures up to 600°C. The ΔE_V values are then extracted from the shift of the core levels for the heterojunction samples with the thin NiO overlayers [38,39]. The XPS spectrum indicated the nickel was in the 2+ oxidation state in the NiO. We used the Kraut method described earlier to measure the valence band offsets by observing the shift of the core levels from the α-Ga₂O₃ when NiO was deposited. The XPS spectra from which we extracted the core energy differences to VBM for thick NiO layers after different annealing temperatures are shown in Figure 5. The valence band maxima values were determined by linear extrapolation of the leading edge to the baseline of the valence band spectra. The corresponding VBMs are shown in Table 2. The error bars in the different binding energies were combined in a root sum square relationship to determine the overall error bars in the valence band offsets [33]. Note that sample charging is not an issue when determining band offsets since we only need peak core shift deltas, which will shift all binding energies by the same amount. We also did not observe any differential charging,

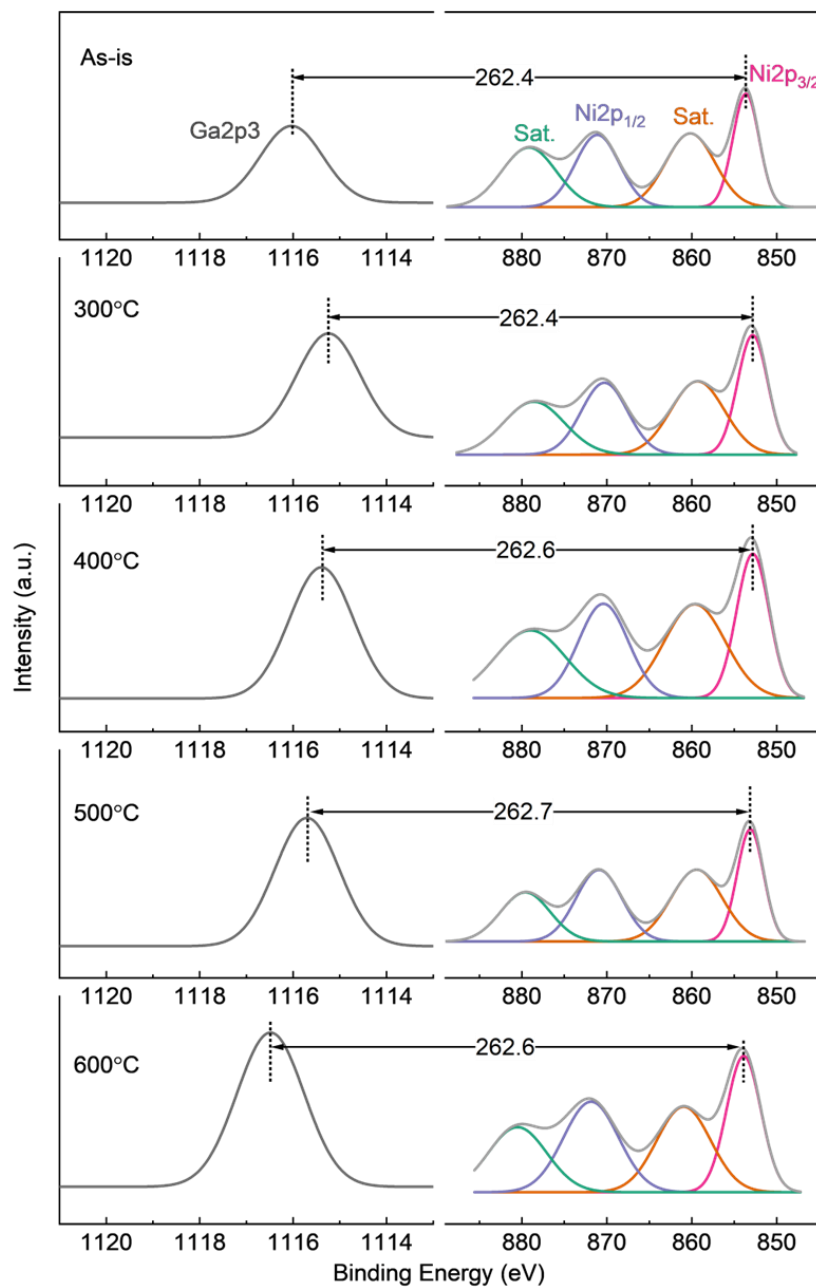which could shift peaks by different amounts and could potentially be a large source of error.

Figure 4. Δ Core Level energies for interfaces of thin NiO/ α-Ga$_2$O$_3$ as-is and annealed at different temperatures.
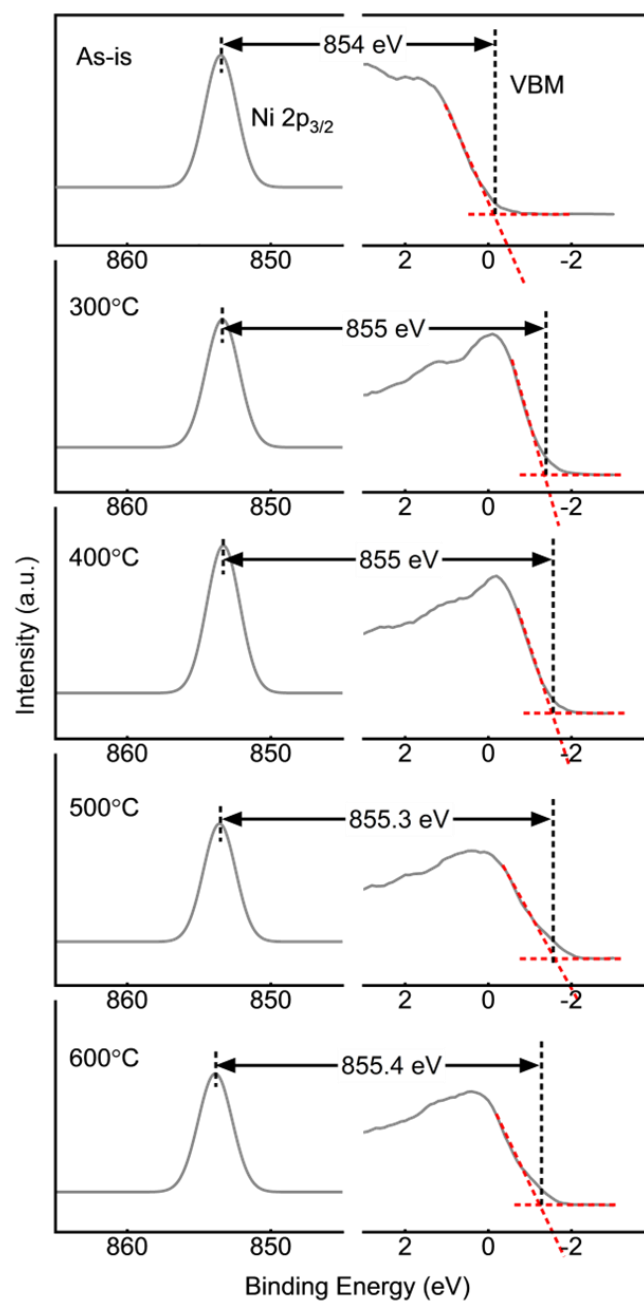
Figure 5. Core -VBM energies for thick NiO film as-deposited and annealed at different temperatures.

Table 2. Core level data measured by XPS data as a function of post-deposition annealing temperature.

	Reference NiO			Thin NiO on α-Ga$_2$O$_3$			
	VBM	Core Level Peak (Ni 2p$_{3/2}$)	Core - VBM	Core Level Peak (Ga 2p$_{3/2}$)	Core Level Peak (Ni 2p$_{3/2}$)	△Core level	Valence band offset
As-is	-0.6	853.4	854	1116	853.6	262.4	2.8
300°C	-1.8	853.2	855	1115.2	852.8	262.4	3.8
400°C	-1.9	853.1	855	1115.4	852.8	262.6	4
500°C	-1.9	853.4	855.3	1115.7	853	262.7	4.4
600°C	-1.7	853.7	855.4	1116.4	853.8	262.6	4.4

Figure 6 shows the band alignment of NiO on α-Ga$_2$O$_3$ after the different annealing temperatures. Note that there is a staggered type II alignment across the entire annealing range investigated, which is advantageous for hole injection The valence band offsets were 2.8± 0.30 eV for the as-deposited heterojunction, 3.8 ± 0.35 eV after annealing at 300°C, 4.0 ± 0.35 eV after annealing at 400°C and 4.4 ± 0.4 eV for annealing at 500°C and at 600°C. The respective conduction band offsets vary from 1.6-3.04 eV. Note that the band offsets increase monotonically with annealing temperature and will not provide any barrier to electrons moving into the Ga$_2$O, suggesting that NiO may not work as an effective guard-ring material on α- Ga$_2$O$_3$ rectifiers. Thus, it would be necessary to have separate electrode materials for hole injection (NiO) and mitigation of peak electric fields. Standard metals such as Au or Ni might be superior choices for the guard ring

fabrication [47]. While both vertical Schottky rectifiers and heterojunction diodes with Rh$_2$O$_3$ [48], Ir$_2$O$_3$ [24,25] or (Ir$_x$Ga$_{1-x}$)$_2$O$_3$ [49] based on α-Ga$_2$O$_3$ have been reported, there has been little development of edge termination methods for alpha-polytype devices [47].

It is also important to note that the band alignment results were independent of the NiO thickness over the range we examined, which was 3-7 nm. Of course, this is limited the need to probe through the layer to measure the core levels in the underlying Ga$_2$O$_3$.

Figure 6. Schematic of band alignments for NiO/α-Ga$_2$O$_3$ as a function of post-deposition annealing temperature.

While annealing a sputtered material may change its crystallinity, preliminary STEM measurements on the NiO did not show significant structural changes with annealing, and it is difficult to quantify interfacial changes due to both materials being oxides, so that diffusion of oxygen cannot be quantified. However, this does suggest that changes in point defect population play a strong role in the changes in band alignment. This is reflected in the changes in bandgap of the NiO with annealing. The crystallinity and defect and carrier concentrations under different annealing temperatures could also play an important role in determining the band alignments, as in the α-Ga$_2$O$_3$/a-Ir$_2$O$_3$ heterojunction [29]. However, such a study is beyond the scope of the current work, which focusses on the XPS results, and some TEM after 300˚C annealing. Future work will focus on the structural and electrical changes in the NiO under different annealing temperatures.

III. SUMMARY AND CONCLUSIONS

The band alignment of NiO/α-Ga$_2$O$_3$ interfaces and how this varies with annealing temperature has been determined and shows potential for realizing p-n junction power devices based on the alpha polytype of Ga$_2$O$_3$. The type II staggered alignment is retained up to 600°C, which is a practical thermal budget for fabrication of power rectifiers. The results for the NiO on α-Ga$_2$O$_3$ show the same general trends as for the same heterojunction on β-Ga$_2$O$_3$, but an added issue with the former is the limited thermal stability of the alpha polytype. IrO$_x$ also has a staggered gap, type-II alignment with α-Ga$_2$O$_3$ with valence- and conduction-band offsets of 3.34 eV and 1.04 eV, respectively,

16

of the same general magnitude as NiO. It will be interesting to see valence band offsets for other p-type oxides on α-Ga$_2$O$_3$.

ACKNOWLEDGMENTS

AUTHOR DECLARATIONS

Conflicts of Interest

The authors have no conflicts to disclose

DATA AVAILABILITY

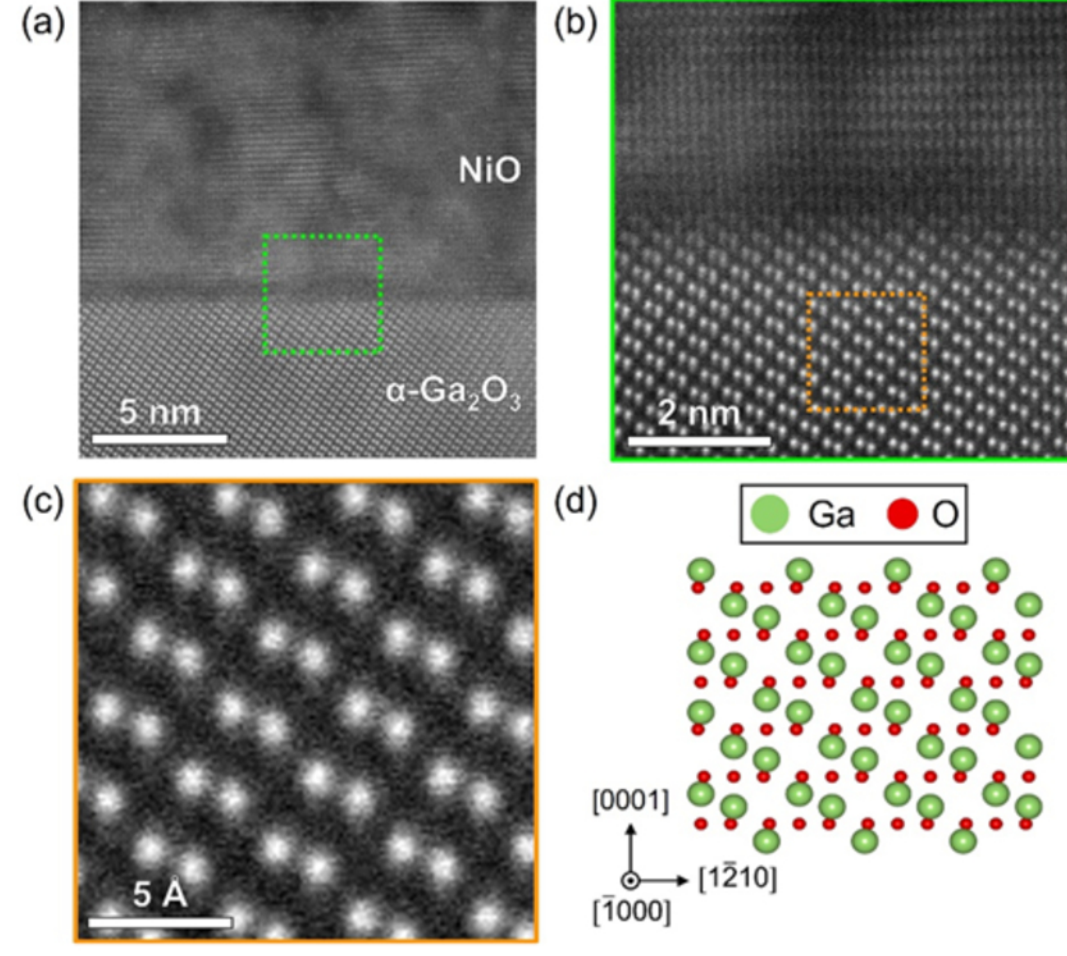All data that support the findings of this study are included within the article.
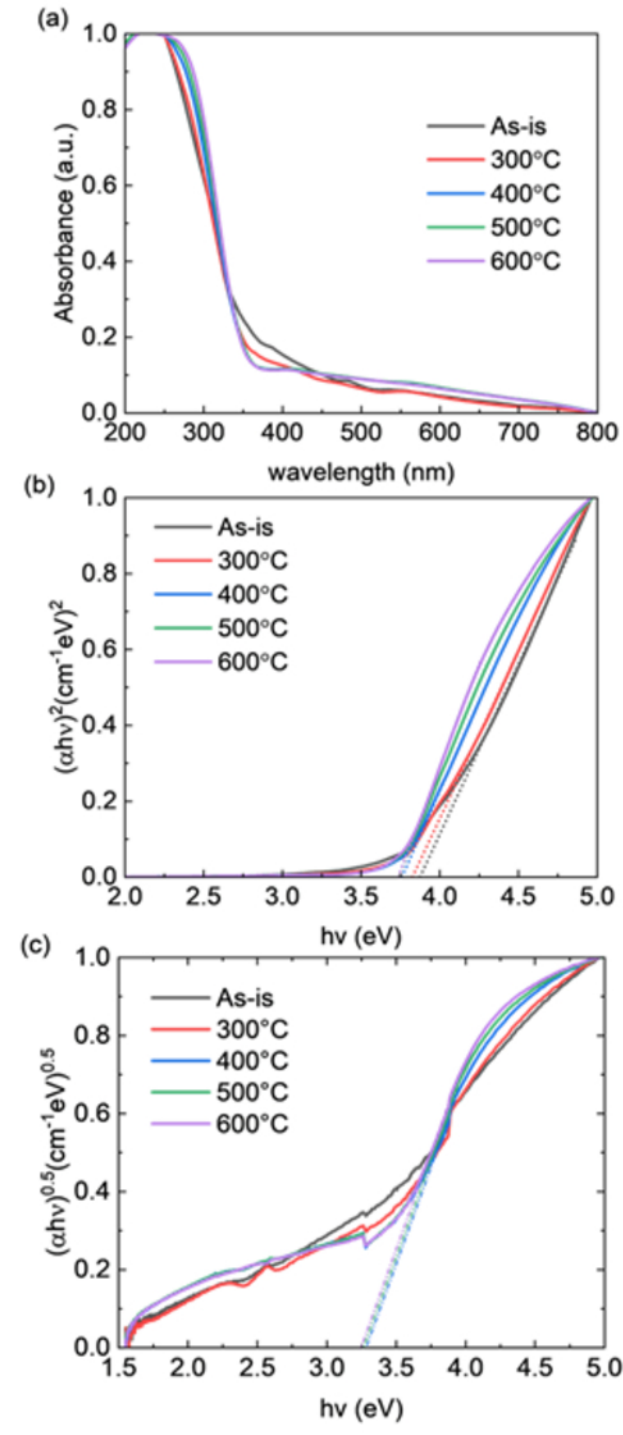
REFERENCES

[1] D. E. Ahmadi and Y. Oshima, J. Appl. Phys. **126**, 160901 (2019).

[2] Takuya Maeda, Mitsuru Okigawa, Yuji Kato, Isao Takahashi, and Takashi Shinohe, AIP Adv. **10**, 125119 (2020).

[3] A. Hassa, P. Storm, M. Kneiß, D. Splith, H. von Wenckstern, M. Lorenz and M. Grundmann, Phys. Status Solidi B, **258**, 2000394 (2021).

[4] H. Zhang, L. Yuan, X. Tang, J. Hu, J. Sun, Y. Zhang, Y. Zhang, and R. Jia, IEEE T. Power Electr. **35**, 5157 (2020).

[5] A. Y. Polyakov, V. I. Nikolaev, E. B. Yakimov, F. Ren, S. J. Pearton, and J. Kim, J. Vac. Sci. Technol. A **40**, 020804 (2022).

[6] Zhengpeng Wang, Xuanhu Chen, Fang-Fang Ren, Shulin Gu and Jiandong Ye, J. Phys D: Appl. Phys, **54**, 043002 (2021).

[7] C. Cora, Z. Fogarassy, R. Fornari, M. Bosi, A. Rečnik, and B. Pecz, Acta Mater.**183**, 216 (2020).

[8] A. F. M. A. U. Bhuiyan, Z. Feng, J. M. Johnson, H.-L. Huang, J. Sarker, M. Zhu, M. R. Karim, B. Mazumder, J. Hwang, and H. Zhao, APL Mater. **8**, 031104 (2020).

[9] M. Hilfiker, U. Kilic, M. Stokey, R. Jinno, Y. Cho, H. G. Xing, D. Jena, R. Korlacki, and M. Schubert, Appl. Phys. Lett. **119**, 092103 (2021).

[10] K. Uno, R. Jinno, and S. Fujita, J. Appl. Phys. **131**, 090902 (2022).

[11] J. A. Spencer, A. L. Mock, A. G. Jacobs, M. Schubert, Y. Zhang, and M. J. Tadjer, Appl. Phys. Rev**. 9,** 011315 (2022).

[12] D. Yang, B. Kim, T. H. Eom, Y. Park, and H. W. Jang, Electron. Mater. Lett.**18**, 113 (2022).

[13] R. Schewski, G. Wagner, M. Baldini, D. Gogova, Z. Galazka, T. Schulz, T. Remmele, T. Markurt, H. von Wenckstern, M. Grundmann, O. Bierwagen, P. Vogt, and M. Albrecht, Appl. Phys. Express **8**, 011101 (2015).

[14] M. Kracht, A. Karg, M. Feneberg, J. Bläsing, J. Schörmann, R. Goldhahn, and M. Eickhoff, Phys. Rev. Appl. **10,** 024047 (2018).
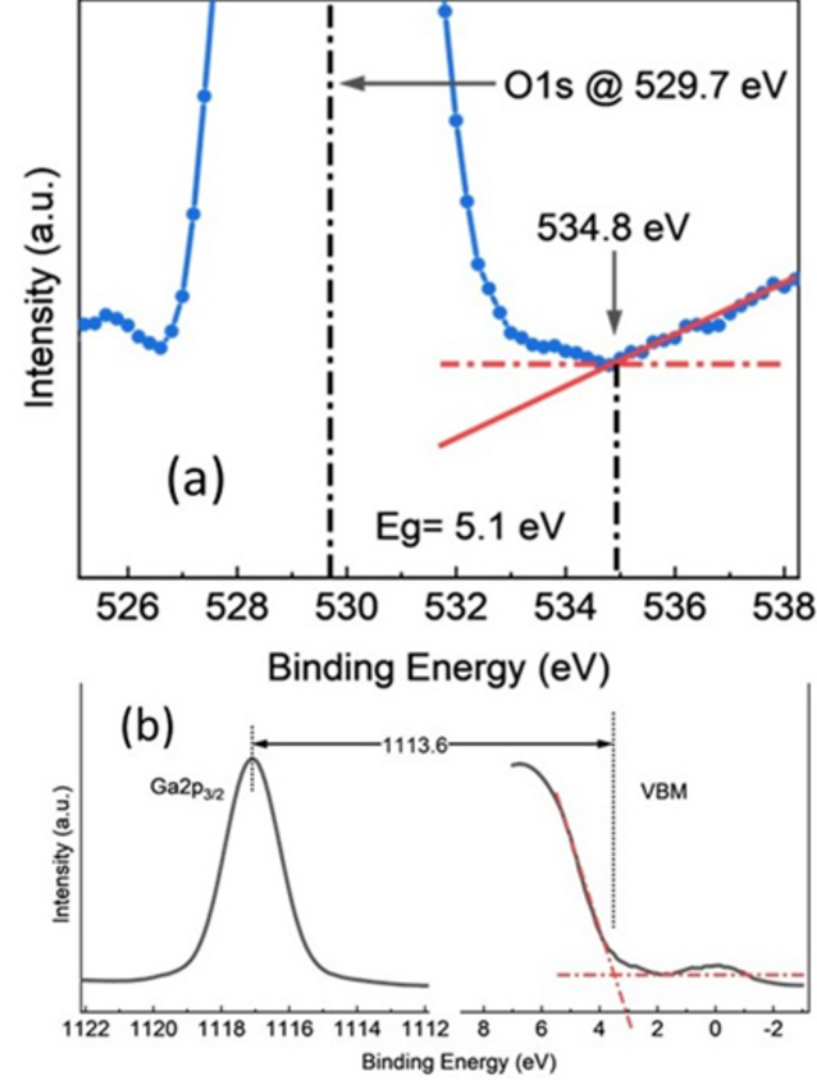
[15]Y. Oshima, K. Kawara, T. Shinohe, T. Hitora, M. Kasu, and S. Fujita, APL Mater. **7**, 022503 (2019).

[16]K. Kawara, Y. Oshima, M. Okigawa, and T. Shinohe, Appl. Phys. Express **13**, 075507 (2020).

[17]Andrew Venzie, Amanda Portoff, W. Beall Fowler, Michael Stavola, Dae Woo Jeon, Jihyun Kim and S. J. Pearton, Appl. Phys. Lett. **120**, 192101 (2022).

[18]Alexander Y. Polyakov, Vladimir I. Nikolaev, Igor N. Meshkov, Krzysztof Siemek, Petr B. Lagov, Eugene B. Yakimov, Alexei I. Pechnikov, Oleg S. Orlov, Alexey A. Sidorin, Sergey I. Stepanov, Ivan V. Shchemerov, Anton A. Vasilev, Alexey V. Chernykh, Anton A. Losev, Alexandr D. Miliachenko, Igor A. Khrisanov, Yu.S. Pavlov, U.A. Kobets and S. J. Pearton, J. Appl. Phys. **132**, 035701 (2022).

[19]A. Sharma and U. Singisetti, Appl. Phys. Lett. **118**, 032101 (2021).

[20]A. Segura, L. Artus, R. Cusco, R. Goldhahn, and M. Feneberg, Phys. Rev. Mater. **1**, 024604 (2017).

[21]M. Hilfiker, R. Korlacki, R. Jinno, Y. Cho, H. G. Xing, D. Jena, U. Kilic, M. Stokey, and M. Schubert, Appl. Phys. Lett. **118**, 062103 (2021).

[22]M. Feneberg, J. Nixdorf, M. D. Neumann, N. Esser, L. Artus, R. Cusco, T. Yamaguchi, and R. Goldhahn, Phys. Rev. Mater. **2**, 044601 (2018).

[23]M. Stokey, R. Korlacki, M. Hilfiker, S. Knight, S. Richter, V. Darakchieva,R. Jinno, Y. Cho, G. H. Xing, D. Jena, Y. Oshima, K. Khan, E. Ahmadi, and M. Schubert, Phys. Rev. Mater. **6,** 014601 (2022).

[24]S. I. Kan, S. Takemoto, K. Kaneko, I. Takahashi, M. Sugimoto, and T. Shinohe, Appl. Phys. Lett. **113**, 212104 (2018).

[25]J. G. Hao, H. H. Gong, X. H. Chen, Y. Xu, F. F. Ren, and S. L. Gu, Appl. Phys. Lett. **118**, 261601 (2021).

[26]J. P. McCandless, C. S. Chang, K. Nomoto, J. Casamento, V. Protasenko, P. Vogt, D. Rowe, K. Gann, S. T. Ho, W. Li, R. Jinno, Y. Cho, A. J. Green, K. D. Chabak, D. G. Schlom, M. O. Thompson, D. A. Muller, H. G. Xing, and D. Jena, Appl. Phys. Lett. **119**, 062102 (2021).

[27]J. G. Hao, H. H. Gong, X. H. Chen, Y. Xu, F.-F. Ren, S. L. Gu, R. Zhang, Y. D. Zheng, and J. D. Ye, Appl. Phys. Lett. **118**, 261601 (2021).

[28]S. I. Kan, S. Takemoto, K. Kaneko, I. Takahashi, M. Sugimoto, T. Shinohe, and S. Fujita, Appl. Phys. Lett. **113**, 212104 (2018).

[29]Dohwan Jung, Yoonseo Jang, Prakash R. Sultane, Christopher W. Bielawski, Jungwoo Oh, J. Alloys Compd, **922**, 166197 (2022).

[30]Xinyi Xia, Jian Sian Li, Chao Ching Chiang, Timothy Jinsoo Yoo, Fan Ren, Honggyu Kim and S.J. Pearton, J. Phys. Appl. Phys. D **55**, 385105 (2022).

[31]H. H. Gong, X. H. Chen, Y. Xu, Y. T. Chen, F. F. Ren, B. Liu, S. L. Gu, R. Zhang, and J. D. Ye, IEEE T. Electron Dev. **67**, 3341 (2020).

[32]Sahadeb Ghosh, Madhusmita Baral, Rajiv Kamparath, S. D. Singh and Tapas Ganguli, Appl. Phys. Lett. **115**, 251603 (2019).

[32]X. Lu, Xianda Zhou, Huaxing Jiang, Kar Wei Ng, Zimin Chen, Yanli Pei, Kei May Lau and Gang Wang, IEEE Electr. Device L., **41**, 449 (2020).

[34]Jiaye Zhang, Shaobo Han, Meiyan Cui, Xiangyu Xu, Weiwei Li, Haiwan Xu, Cai Jin, Meng Gu, Lang Chen and Kelvin H. L. Zhang, ACS Appl. Electron. Mater. **2**, 456 (2020).

[35]Hoki Son and Dae-Woo Jeon, J. Alloy Compd, **773**, 631(2019).

[36]Joseph A. Spencer, Alyssa L. Mock, Alan G. Jacobs, Mathias Schubert, Yuhao Zhang, and Marko J. Tadjer, Appl. Phys Rev **9**, 011315 (2022).

[37]L. Mattheiss, Phys. Rev. B **5**, 290 (1972).

[38]R. Powell and W. Spicer, Phys. Rev. B. **2**, 2182 (1970).

[39]B.D. Viezbicke, S. Patel, B.E. Davis, D.P. Birnie, Phys. Status Solidi B, **252**, 1700 (2015).

[40]Timothy A. Morgan, Justin Rudie, Mohammad Zamani-Alavijeh, Andrian V. Kuchuk, Nazar Orishchin, Fikadu Alema, Andrei Osinsky, Robert Sleezer, Gregory Salamo, and Morgan E. Ware, ACS Appl. Mater. Inter. **14**, 33944 (2022).

[41]E. A. Kraut, R. W. Grant, J. R. Waldrop, and S. P. Kowalczyk, Phys. Rev. Lett., **44**, 1620 (1980).
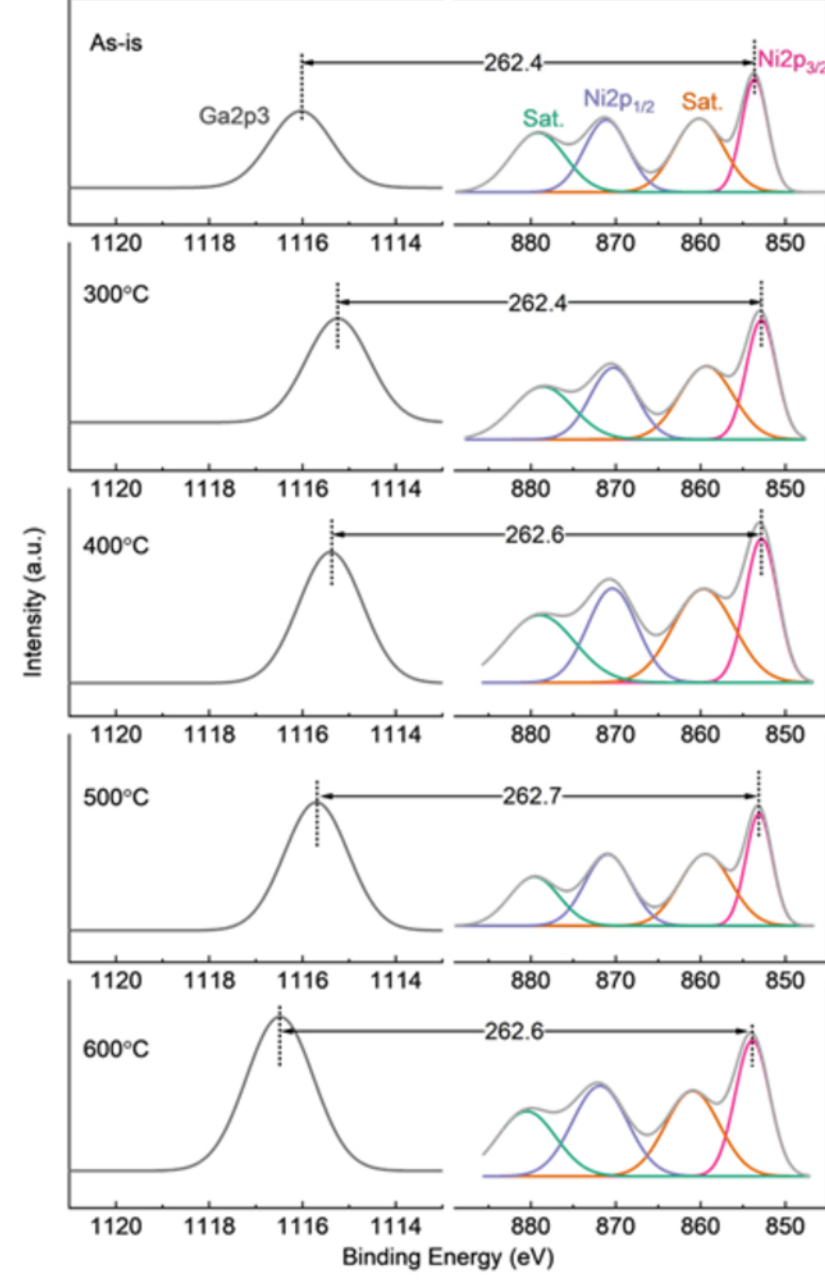
[42]Scott A. Chambers, Le Wang, and Donald R. Baer, J. Vac. Sci Technol. A **38**, 061201 (2020).

[43]Grzegorz Greczynski and Lars Hultman, J. Appl. Phys. **132**, 011101 (2022).

[44]Grzegorz Greczynski, Lars Hultman, Science Talks **1**, 100007 (2022).

[45]C. Fares, F. Ren, Max Knessl, H. von Wenckstern, M. Grundmann and S.J. Pearton, chapter 9 in Wide Bandgap Semiconductor Based Electronics, ed F. Ren and S.J. Pearton (IOP Publishing, Bristol, (2020).

[46]D. C. Hays, B.P. Gila, S. J. Pearton and F. Ren, Appl. Phys. Rev., **4**, 021301 (2017).

[47]Xinyi Xia, Jian-Sian Li, Chao-Ching Chiang, Timothy Jinsoo Yoo, Fan Ren, Honggyu Kim, and S. J. Pearton, J. Vac. Sci. Technol. A **40**, 053401 (2022).

[48]D. Yang, B. Kim, T.H. Eom, Yongjo Park and Ho Won Jang, Electron. Mater. Lett. **18**, 113 (2022).

[49]K. Kaneko, S. Fujita and T. Hitora, Jpn. J. Appl. Phys. **57**, 02cb18 (2018).

[50]Kentaro Kaneko, Yasuhisa Masuda, Shin-ichi Kan, Isao Takahashi, Yuji Kato, Takashi Shinohe, and Shizuo Fujita, Appl. Phys. Lett. **118**, 102104 (2021).